Probing Plasmon-Induced Chemical Mechanisms by Free-Radical Nanophotopolymerization

Farid Kameche, Wajdi Heni, Siham Telitel, Loïc Vidal, Sylvie Marguet, Ludovic Douillard, Céline Fiorini-Debuisschert, Renaud Bachelot, Olivier Soppera

Probing Plasmon Induced Chemical Mechanisms by Free Radical NanoPhotopolymerization

Farid Kameche,[1,2] Wajdi Heni,[1,2] Siham Telitel,[1,2] Loïc Vidal,[1,2] Sylvie Marguet,[3] Ludovic Douillard,[4]

Céline Fiorini-Debuisschert,[4] Renaud Bachelot,[5,6] and Olivier Soppera.[1,2]*

1. Université de Haute-Alsace, CNRS, IS2M UMR 7361, F-68100 Mulhouse, France

2. Université de Strasbourg, France

3. Université Paris-Saclay, CEA, CNRS, NIMBE, F-91191 Gif-sur-Yvette, France

4. Université Paris-Saclay, CEA, CNRS, SPEC, F-91191 Gif-sur-Yvette, France

5. Light, nanomaterials, nanotechnologies (L2n) Laboratory, CNRS ERL 7004, Université de Technologie de Troyes, F-10004 Troyes, France

6. Sino-European School of Technology, Shanghai University, 200444 Shanghai, China

* Contact : olivier.soppera@uha.fr

Abstract

Localized surface plasmon induced photopolymerization of free radical acrylate monomers is an efficient, smart and versatile method for preparing metal/polymer hybrid nanoparticles with accurate control of the thickness and spatial distribution of the polymer on the nanoparticle surface. Despite a growing number of practical demonstrations, the mechanism leading to polymerization of the acrylate monomer by LSPR is still controversial. It could be related either to a photochemical mechanism enhanced by electromagnetic hot spots (enhanced near-field), thermoplasmonic (photothermal heating) or electrochemical (*via* hot-carrier injection) mechanisms, as proposed in different studies. After developing a high resolution charac-

terization method based on transmission electron microscopy and by tuning the photopolymer composition and the irradiation conditions, the LSPR-induced physicochemical mechanism is revealed. We demonstrate that the photochemical pathway is the main mechanism under the mild irradiation conditions chosen for this process. In a more general way, photopolymerization proves to be a powerful tool to investigate the coupling between metal nanostructures and organic moieties.

Introduction

Metal nanoparticles (NPs) are widely studied because of their specific properties, opening new opportunities in biological,[1–5] catalysis[6–8] and optical[9–11] applications. These original properties arise from localized surface plasmon resonances (LSPR). A LSPR is observed when a light wave is trapped within metallic NPs smaller than the wavelength of the incident light, resulting in a strong interaction between the light and the electrons of the NPs conduction band.[12–14] This strong interaction generates a collective oscillation of the electrons and thus an electromagnetic field. The generated electromagnetic field is locally confined and presents a strongly enhanced intensity compared to the incident field intensity.

By coupling with organic molecules, these metallic nanostructures produce hybrid nanoparticles (HNPs) with novel applications in analytical chemistry, sensing, photocatalysis, photovoltaics or nanomedicine. New or enhanced specific properties such as light generation through photoluminescence[15,16], biological recognition[17] or optical sensing[18,19] can indeed be observed for HNPs. Such interest has justified the development of many preparation techniques with different levels of control and complexity.[20–24] The molecules can mainly be adsorbed at the surface of the NP or be covalently linked *via* self-assembly strategies due to functional groups with high affinity to metals (such as thiol or amines). In the case of macromolecules, two main strategies are possible:[25] polymer chains can be prepared *ex situ* and grafted onto the surface of the NPs, or macromolecules can be prepared directly on the NP surface, starting from monomers or oligomers, by polymerization initiated at the surface of the NP. This latter strategy is interesting because the (photo)catalytic properties of the NPs can be exploited to trigger the process, especially when using LSPR light-induced processes.[26–29] In this case, spatiotemporal control of the reaction can be

2

achieved, leading to precise grafting of the polymer at the NP surface. Based on this concept, several examples of free radical photopolymerization,[27,28,30] including two-photon photopolymerization, reversible deactivation radical polymerization (RDRP)[30–32] and oxidative polymerization,[33,34] have been proposed recently.

Despite these convincing proofs of concept, the mechanisms underlying the origin of LSPR polymerization remain unclear and controversial. In fact, three different mechanisms could be at play to interpret the formation of HNPs. They are schematically depicted in **Figure 1**.
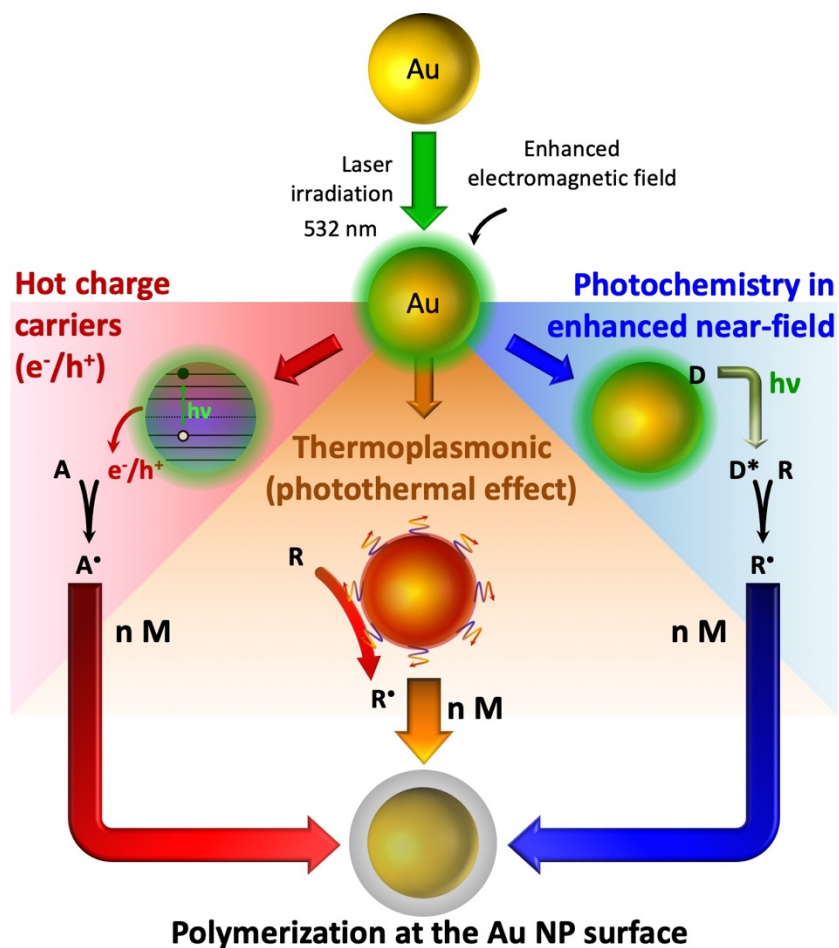
Figure 1: Schematic of the three main pathways to trigger polymerization by LSPR with a circular polarization of incident light. From left to right, (i) hot charge carriers, (ii) thermoplasmonic (photothermal effects) or/and (iii) photochemistry in enhanced near-field. (A: carrier acceptor, M: monomer, D: dye, R: radical generator).

On the left side of **Figure 1**, the hot carrier process is based on a redox reaction between carriers (electrons or holes) generated at the surface of metallic NPs following light excitation and an electron acceptors (A) present in the vicinity of the NP. The formed radical can then react with other molecules or monomers to initiate polymerization.[34–36] Diazonium salts have been grafted onto Au NPs and the electroreduction of the salts was achieved through hot electrons.[37,38] As in the case of the above described photochemical reactions, anisotropic electropolymerization can be obtained by controlling the shape of the NPs and/or the light excitation wavelength and polarization. Hot electrons have also been used to catalyze reactions such as the oxidation of isopropanol to acetone[39,40] or the oxidation of CO.[41] Recently, Wang *et al.* used this concept to achieve polymerization. They demonstrated the polymerization of styrene, divinylbenzene and methyl methacrylate with a spatial localization at the hot spots where hot carriers are expected to be generated.[33] Hot holes can also be exploited to initiate oxidative polymerization. Electrooxidation of aniline to polyaniline[42] and pyrrole to polypyrrole[43] was recently described. In these cases, the mechanism of polymerization is explained by the formation of radical cations involving the holes created by plasmon excitation. Such radicals can induce electropolymerization to form conductive polymers.

A second pathway to initiate polymerization at the nanoscale relies on an increase in temperature, which is also known as the thermoplasmonic effect (center part of **Figure 1**). Ultimately, the damping of a plasmon resonance causes the particle to heat up on a characteristic time scale of 0.1 - 10 ns depending on the thermal diffusivity of the surrounding environment.[44] Heating can decompose radical generator molecules (R) or even monomers (M) to start polymerization. The temperature in the vicinity of the NPs is different than the temperature of the bulk medium, which is especially true when the NPs are illuminated with a continuous wavelength laser.[14,45–49] The local increase in the temperature can be sufficient to trigger a chemical reaction. Several research teams have used simulations to evaluate the temperature that can be reached in the vicinity of a NP depending on irradiation conditions (irradiance of the incident light, irradiated area, light wavelength, nature and morphology of the NP, NP surface density, nature of the surround-

4

ing medium, the substrate, etc.). The near-field temperature can oscillate between room temperature and several hundred degrees. Fedoruk *et al.* achieved a micrometric polymerization of dimethylsiloxane by using only Au NPs deposited on a glass cover slip and a laser emitting at 532 nm.[50] The temperature at the surface of the Au NPs was 340°C, which was sufficient to trigger polymerization of dimethylsiloxane after a few seconds. Moreover, these researchers were also able to control the growth of the polymer by controlling the irradiation conditions. Walker *et al.* grafted a thiol-functionalized enediyne onto an Au NP surface, and radical polymerization was achieved by photothermal reactions.[29] Ag NPs were also used to thermally trigger the polymerization of caprolactam into nylon-6.[51]

The right side of **Figure 1** describes the photochemical pathway: LSPR excitation generates a confined and enhanced electromagnetic field in the vicinity of NPs. A dye (D) absorbing at the excitation wavelength is promoted to its excited state and reacts with a coinitiator (R) to form radicals that induce polymerization of the monomer (M). Due to LSPR, the near-field intensity is thus locally higher than the far-field intensity, which can be used to overpass the reaction threshold and thus start a photochemical reaction limited to the vicinity of the electromagnetic hot-spots. Free radical photopolymerizations indeed exhibit this threshold behavior, which makes it possible to specifically localize the polymer immobilization around the NPs.

In this paper, we focus on a photopolymer system that is known to follow a free radical photopolymerization mechanism in the far field excitation conditions. The reference system is composed of a Norrish II photoinitiating system (Eosin Y and MDEA) and a triacrylate monomer. As shown below, it is used under very soft irradiation conditions, which are just below the threshold conditions necessary to obtain far-field polymerization.

We perform a systematic investigation of the important parameters of the system to identify the relevant mechanism involved together with possible interplay. This study is based on the development of a new methodology based on transmission electron microscopy (TEM). The samples are prepared directly on a TEM grids and can be analyzed after each step of the process. TEM characterization provides a direct

high-resolution visualization of the HNPs to precisely observe and estimate its characteristics. Moreover, it provides a 3D observation of the HNP with tomography mode and makes it possible to analyze a large number of NPs to obtain a statistical view of the polymerization. Using this strategy, we aim to investigate in detail the process leading to the formation of HNPs by LSPR triggered polymerization.

Experimental
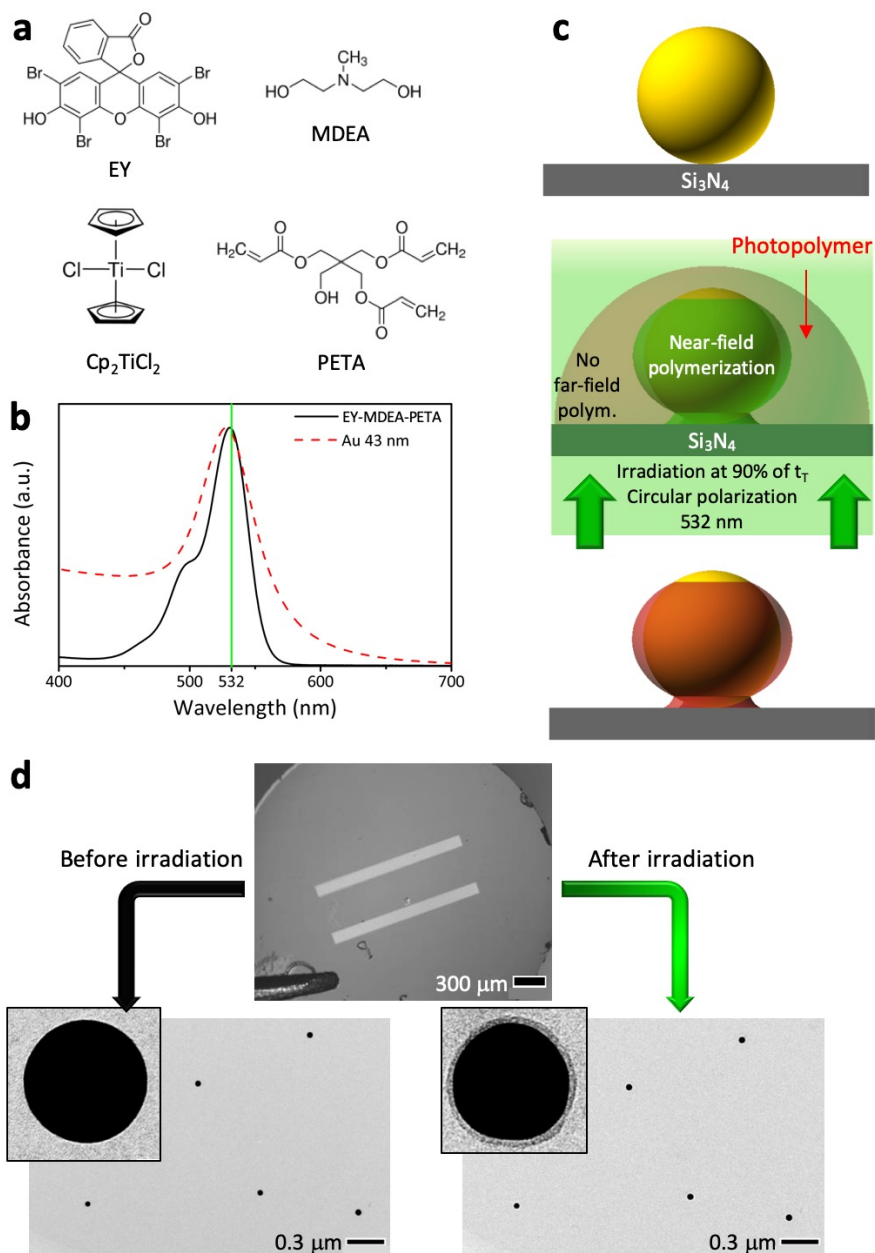
Figure 2: (a) Molecular structure of the molecules used. EY/MDEA and Cp_2TiCl_2 are photoinitiators, PETA is an acrylate monomer. (b) Normalized UV-visible extinction spectra of the formulation and the water solution of 43 nm diameter spherical Au NPs. (c) Scheme of the optical near-field experiment. (d) Optical image of a typical TEM grid used including 2 rectangular slits (1500 µm x 100 µm) (upper line) and two TEM images before and after performing an optical near-field experiment (bottom) with magnification of a single particle (inset).

Preparation of the formulation

The reference formulation is composed of 0.5 wt. % Eosin Y (noted as EY) and 4 wt. % *N*-methyldiethanolamine (noted as MDEA) in pentaerythritol triacrylate (noted as PETA). The EY dye is first added to PETA and stirred until completely dissolved. Afterwards, MDEA is added to the mixture and stirred for a few hours. In some experiments, another photoinitiator was used: bis(cyclopentadienyl)titanium(IV) dichloride (referred to as Cp_2TiCl_2). 0.3 wt. % Cp_2TiCl_2 was simply added to PETA and stirred for a few hours until its dissolution. All the products cited above were obtained from Sigma Aldrich and were used as received. All the molecules are shown in **Figure 2a**, and the normalized absorption spectrum of the reference formulation is plotted in **Figure 2b**.

Preparation of the NPs

Spherical (43 ± 2 nm diameter) and cubic (57 nm and 130 nm edge) Au NPs were prepared by colloidal chemistry using cetyltrimethylammonium bromide (CTAB) as a capping agent.[52–55] The cubes were obtained in the first step, according to an already published protocol.[53,54] They were converted to highly spherical nanospheres in a second step by chemical etching in the presence of $HAuCl_4$ and CTAB. The oxidation of Au nanocrystals with Au(III)-CTAB complexes was indeed shown to occur preferentially at surface sites with high curvatures. The extinction spectrum of the solution of spherical Au NPs is given in **Figure 2b**.

Characterization of the samples

The samples were all prepared on silicon TEM grids with two rectangular slits (1500 μm x 100 μm) covered on one face with a 50 nm-thick Si_3N_4 membrane (supplied by TEDPELLA). Two different TEM instruments were used: a PHILIPS CM200 for characterizing samples after the photopolymerization process and a high-resolution TEM (HRTEM) ARM200F JEOL equipped with a double tilt sample holder for the tomographic experiment providing tilted images (0° to 40°).

All the resulting images were characterized with ImageJ software to measure the thickness of the polymer layer (denoted as d_{layer}).

LSPR polymerization process

Before carrying out LSPR polymerization, the threshold time t_T in far field illumination must be determined. It corresponds to the minimum time required to trigger the photopolymerization at a given power. A bare TEM grid was placed in the path of a frequency-doubled Nd-YAG laser (532 nm, 6 W, continuous wave, VERDI model from Coherent Inc.). The setup was designed to generate collimated illumination with a homogeneous power density over the area of interest (typ. a few mW/cm^2 on 1 cm^2) and with circular polarization (**Figure S1** in the Supporting Information (SI)). A drop of the formulation (approximately 4 μL) was then deposited onto the TEM grid and the whole system was irradiated at a fixed power and time. Irradiation time is controlled with an automatic shutter. Such conditions correspond exactly to the conditions used later for optical near-field polymerization. The sample was then rinsed with ethanol and observed by optical microscopy to detect the eventual presence of the polymer on the surface of the TEM grid. The threshold t_T is defined as the minimum irradiation time (for a given excitation power density) enabling polymerization.

The preparation of the HNPs is depicted in **Figure 2c**. TEM grids were functionalized with a self-assembled monolayer of (3-aminopropyl)triethoxysilane (APTS, from Sigma-Aldrich) to firmly graft the NPs on the surface of TEM grids. The solution of Au NPs was centrifuged and washed to remove excess

surfactant. Afterwards, it was deposited on functionalized TEM grids by drop casting, and a UV-ozone treatment was used to remove the remaining surfactant after drying of the water solution.

Once ready, the TEM grids were placed on the optical setup described above. A drop of the formulation was then deposited onto the TEM grid and the whole system was irradiated. Typically, 90% of the threshold time t_T of the formulation was used to avoid any photopolymerisation in the far field. After irradiation, the sample was rinsed with ethanol and TEM characterization was performed. As shown in **Figure 2d**, which compares the position of the NPs before and after the polymerization process the anchoring of the NPs on the surface was successful. It can also be observed from these images that the TEM grids are free of residues before and after polymerization, showing that the deposition and cleaning procedures are appropriate.

Results and discussion

LSPR polymerization

The reference formulation EY-MDEA-PETA has been demonstrated to be useful in the context of LSPR polymerization[27,28,56,57] and other microfabrication processes[58–60] that rely on its strong absorption at 532 nm. The polymerization is efficient even in the presence of oxygen (**Figure 2d**). The mechanism of the photopolymerization is shown in **Figure S2**. In brief, light excites the EY dye from the fundamental state into a singlet state that is converted to triplet ^{3}EY by intersystem crossing. The MDEA amine reacts with ^{3}EY to form an aminoalkyl radical by electron and proton transfer. Finally, this radical reacts with the acrylate functions of PETA and free-radical polymerization starts. The growth of the polymer is fast due to the high concentration of acrylate functions since the formulation is constituted from the liquid monomer (no solvent). Crosslinking of the trifunctional monomers results in rapid gelification and vitrification of the medium, which stops the conversion of the monomer at approximately 50% conversion.[28,61] The growth of the polymer and most of the reactions described above can also be stopped by reaction with oxygen in the formulation. Indeed, oxygen can react both with the different radicals and/or the triplet state

of EY to stop the process of photopolymerization. In the present case, O_2 quenching is very important for the spatial control of the photopolymerization process at the micro- and nanoscales. It also accounts for the threshold time t_T. At a 2 mW/cm^2 irradiance the photopolymerization threshold is found to be 1.5 s. The LSPR polymerization was thus carried out using an exposure time of 1.35 s corresponding to 90% of the threshold time needed for this power density. Typical TEM images of the NP before and after the experiment are presented in **Figure 3a**.
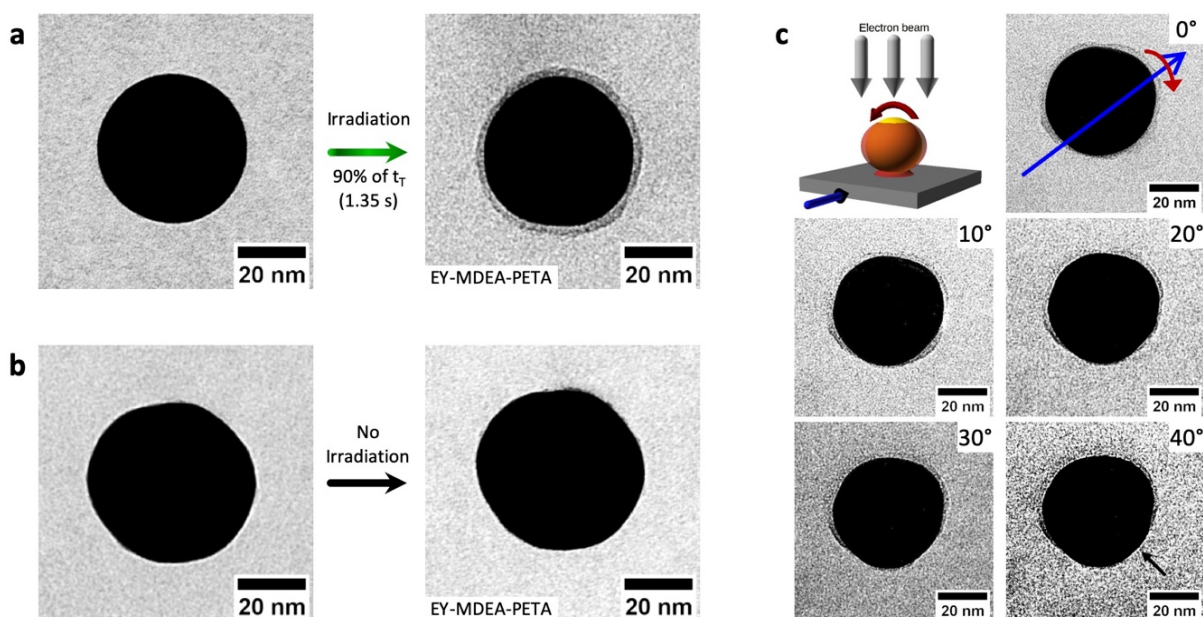
Figure 3: (a) TEM images of 43 nm Au NPs before irradiation and after irradiation at 2.0 mW/cm^2 at 90% of the threshold dose with EY-MDEA-PETA. (b) TEM images of 43 nm Au NPs before and after depositing a drop of formulation and cleaning the sample. No irradiation of this sample was performed. (c) Representation of the HNPs and TEM images of the same NPs after tilting the sample from 0° to 40°. The blue arrows and the red arrows represent respectively the axis rotation and the rotation direction. The black arrow on image at 40° shows the top of the NP after tilting the sample.

A polymer layer of thickness d_{layer} = 2.5 nm can be observed after irradiation. To verify that the layer is due to the irradiation of the NPs in the presence of the formulation, a control sample was prepared by depositing a drop of the formulation on a TEM grid in the presence of NPs but without irradiation. After washing the sample, no changes were observed by TEM on the surface of the NPs (**Figure 3b**). The result obtained with this control experiment confirms that the layer observed on **Figure 3a** is a polymer and not some residual monomer adsorbed on the surface of the NPs (more NPs are presented in **Figure S3**).

TEM provides high-resolution images of the polymer layer, but these images are only planar projections of the object, which results in a loss of information about the spatial distribution of the polymer around the NPs. To determine how the polymer covers the NPs, we performed tomography experiments. TEM images were recorded after tilting the sample from 0° to 40° in 10° intervals (see **Figure 3c**). As the tilt angle increased, the polymer was no longer visible on the side of the particle that corresponds to the top of the NPs (position marked with a black arrow in the image corresponding to 40°). It remains visible at the NP equatorial plane and between the NPs and the substrate. This repartition of the polymer corresponds well to the distribution of the electromagnetic near field around the NPs upon circular polarization excitation. It also confirms the results obtained recently with another photoinitiating system.[30]

At this stage of the study, the possibility of inducing a photopolymerization reaction that remains confined around the NPs and that accurately reproduces, at the nanometric scale, the distribution of the electromagnetic field is thus verified. In the following sections, the above-mentioned three types of mechanisms (**Figure 1**) are considered, and variations in photonic and chemical conditions are used to elucidate the mechanism at play.

Hot charge carriers

We first investigated the possibility of inducing the polymerization of this system by hot carriers generated by the excitation of the NPs. As presented in the introduction, hot carriers can be of two different kinds: electrons or holes. As polymerization is initiated in the EY-MDEA system by the aminoalkyl radical formed from the MDEA, we tested the polymerization with irradiation conditions identical to those

11

described in the previous paragraph but in the absence of EY, as photoinitiator. Thus, the possibility of creating an aminoalkyl radical by the usual photomechanism involving EY in its triplet state by electron transfer is eliminated. In the basic mechanism between EY and MDEA, an electron transfer occurs from MDEA to EY and corresponds to the oxidation of MDEA. An equivalent to this mechanism involving hot carriers produced on the surface of the NPs thus corresponds to a hole transfer from the NP to MDEA (that is equivalent to an electron transfer from MDEA to NP) to produce an aminoalkyl radical capable of initiating the polymerization of acrylate monomers.
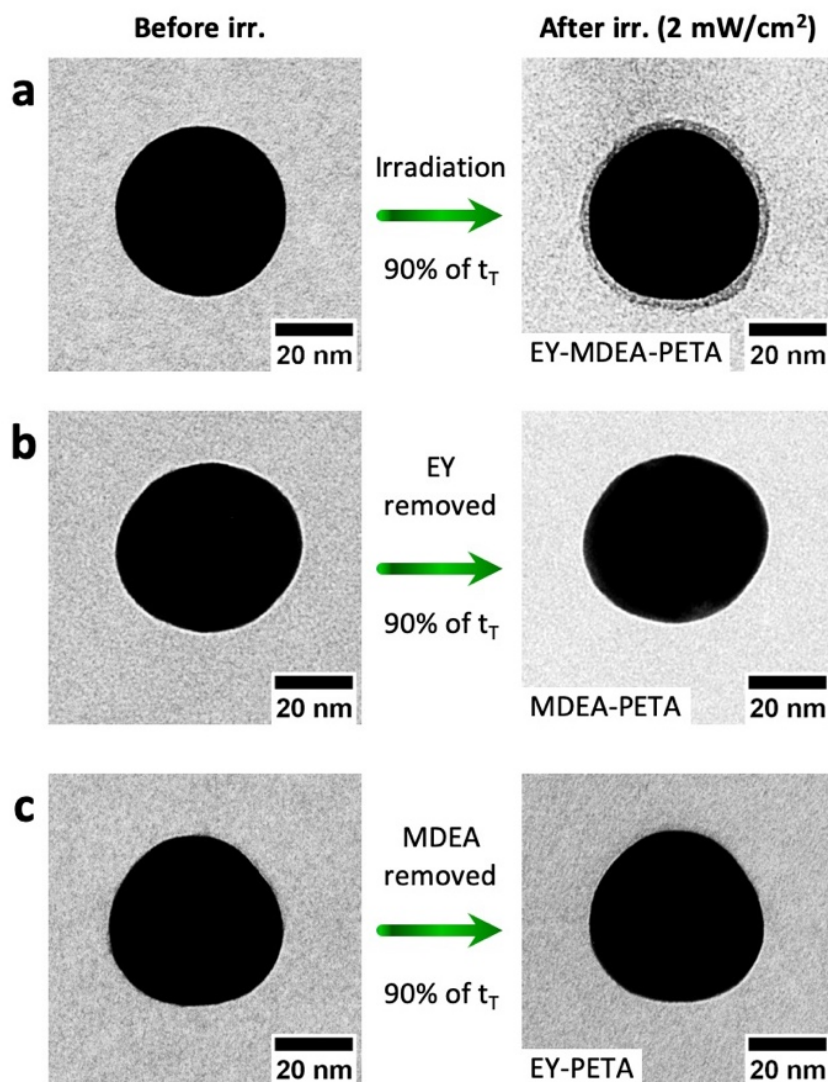
Figure 4: TEM images of 43 nm Au NPs before irradiation and after irradiation at 2.0 mW/cm^2 at 90% of the threshold time (irradiation time 1.35 s) with a formulation comprising (a) EY-MDEA-PETA, (b) MDEA-PETA and (c) EY-PETA.

The results are given in **Figure 4** (more NPs are presented in **Figures S4** and **S5**). A comparison between **Figures 4a** and **4b** clearly shows that polymerization requires the presence of EY in the formulation to be efficient under identical irradiation conditions. Indeed, if EY is removed, no polymer can be observed at the NP surface, suggesting that a mechanism involving hot hole carriers reacting with MDEA to start polymerization is inefficient under the considered "mild" excitation conditions. In **Figure 4c**, we also show that EY used without MDEA cannot initiate polymerization. This excludes the interaction of EY with hot carriers and the direct excitation of the PETA monomer.

Such formulations were also tested with higher irradiation doses. When EY or MDEA was removed from the reference formulation, far-field photopolymerization could not occur, even at 10 times the dose needed to polymerize the reference formulation (15 s at 2.0 mW/cm^2). This makes it possible to considerably increase the irradiation time for these two last formulations.
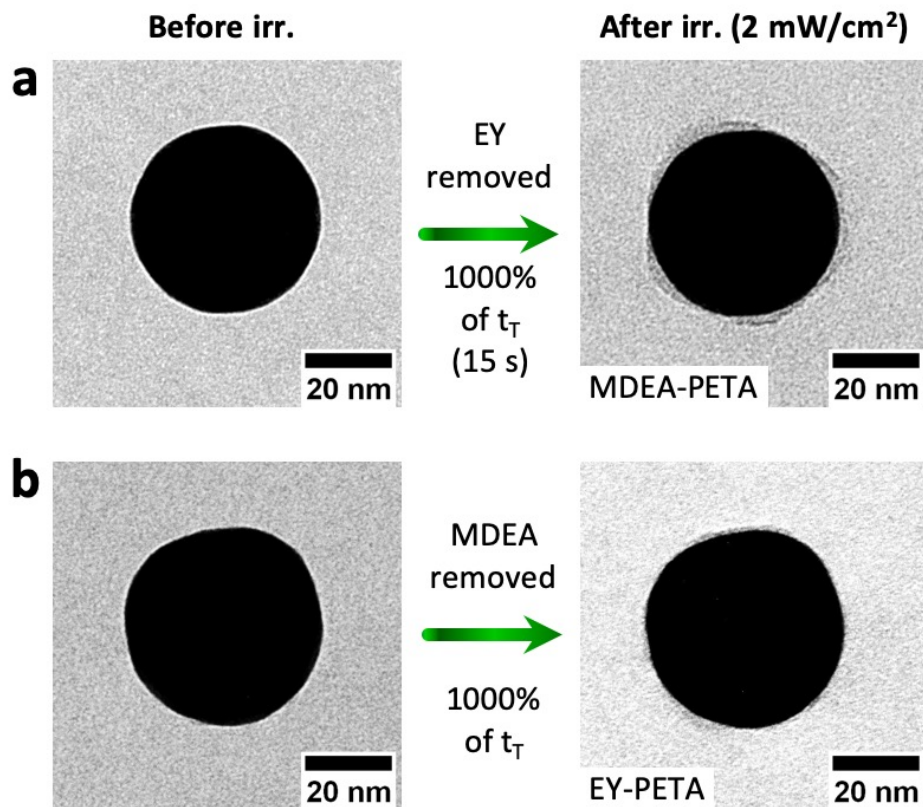
Figure 5: TEM images of 43 nm Au NPs before irradiation and after irradiation at 2.0 mW/cm^2 at 1000% of the threshold time (irradiation time is 10 times the threshold time with EY, e.g. 15 s) with a formulation of (a) MDEA-PETA (no EY) and (b) EY-PETA (no MDEA).

TEM images of the NPs before and after irradiation using the formulation without EY (**Figure 5a)** and without MDEA (**Figure 5b)** are shown (see also **Figures S6** and **S7)**. In **Figure 5a,** the appearance of a 2 nm thick polymer layer surrounding the NP can be observed. The presence of this polymer layer indicates that MDEA is able to initiate polymerization at Au NPs in the absence of EY, when a longer irradiation time is used. The polymerization process is thus much less efficient than that in the presence of both EY and MDEA since the energy needed to reach an equivalent polymer layer is 10 times greater. **Figure 5b** shows that polymerization does not occur for the EY-PETA system without MDEA.

Since MDEA does not absorb at 532 nm, the photoinduced process also involves the NPs. The presence of a polymer can then be explained by the creation of the aminoalkyl radical by an interaction with the hot

holes created on the surface of the NP when the NP is irradiated at resonance. In gold, this mechanism can take place because electron-hole pairs that are formed primarily by interband damping of LSPR (d-sp interband transition) lead to energetics d-holes (lying deep within the d-band) and low-energy electrons.[42,62] Amine are good candidates since they are electron donors and the affinity of amine functional groups for Au also ensures a high concentration of MDEA molecules at the surface of the NPs. The other important point is the high reactivity of the aminoalkyl radicals on the acrylate functional groups.

In conclusion, we thus reveal a reaction pathway involving hot carriers that is parallel to the photochemical pathway but much less efficient.

In the following section, we discuss the role of the thermoplasmonic pathway showing that thermoplasmonic effects can mainly been ruled out.

Thermoplasmonic (photothermal effects)

Several models have been proposed to determine the temperature of metal NPs excited by LSPR.[49,33,63–69] According to the results of these simulations, the temperature at the surface of NPs and in its vicinity can increase from a few degrees to a hundred degrees depending on the experimental conditions. Baffou *et al.* have developed a model based on boundary element method simulations to estimate the variation in the temperature at the surface of Au NP ΔT for continuous wave illumination.[65,69] Ultimately, the variation in temperature ΔT can be expressed, for a nanosphere, as:

$$\Delta T = \frac{\sigma_{abs} I}{4 \pi R k_{med}}$$

where σ_{abs} is the absorption cross section (m^2), I is the light irradiance (W/m^2), R is the radius of the NP (m) and k_{med} the thermal conductivity (W/(m. K)) of the medium surrounding the NP. To achieve a temperature increase of 1 K, for a 50 nm diameter Au nanosphere, an irradiance of 0.1 mW/μm^2 is needed.[70] This value is 7 orders of magnitude greater than the irradiance used in this study, suggesting that the thermal effects are negligible under our conditions. Note that, as illustrated in **Figure 2d**, the surface den-

sity of NPs on the TEM grid is extremely low (with the distance between particles always > 1 μm), there-fore no photothermal collective heating can take place.[63,71] In summary, the temperature increase is expected to be extremely limited in our exposure conditions.

Moreover, this temperature increase must be compared to the temperature needed to polymerize the formulations used in this study. Indeed, it is known that acrylates can start to polymerize at specific temperatures.[72] MDEA is also known to have a relatively low stability with time, which may also be associated with a thermal decomposition mechanism[73,74] that could possibly create radical species able to initiate the polymerization of PETA. For this, we determined the thermal polymerization temperatures for the EY-MDEA-PETA, MDEA-PETA and PETA formulations as follows: a drop of formulation was deposited on a Si substrate heated to a known temperature. Annealing was then carried out for 1 min. Such a long time guaranteed the thermalization of the formulation, and thus, the formulation remained at a high temperature for a time longer than the irradiation time used in LSPR experiments. After annealing, the sample was cooled and rinsed, and the polymerization temperature was defined as the temperature needed to keep the polymer part on the substrate. This simple procedure revealed that the polymerization threshold temperature is 220 ± 10°C for EY-MDEA-PETA, MDEA-PETA and PETA. This reveals first that the thermal polymerization of the formulations can be assigned to the direct decomposition of the PETA monomers upon heating. Second, the temperature needed to start the thermal polymerization is well above the temperature predicted by the numerical models.

In conclusion, thermal polymerization can be excluded in the polymerization mechanism. This is consistent with the absence of a polymer observed in **Figures 4a**, **4b** and **5b.** This result is also in complete agreement with the results shown in **Figure 3c**, which demonstrated anisotropic polymerization around the NP, as expected from near-field simulations under the chosen irradiation conditions (circular polarization). In contrast, thermal phenomena are expected to be uniform across the NPs, which is in contradiction with our observations (see **Figure 3c**). Moreover, the very slight temperature increase predicted by the models cannot account for a modification of the polymerization kinetics that would affect the final result. This leads us to conclude that the photochemical pathway is predominant under our irradiation

conditions and with this photopolymer. The aim of the last part of this paper is to confirm this conclusion with additional experiments.

Photopolymerization

Different power densities were used to determine whether the polymerization efficiency can be correlated to this parameter, which should be the case for a free radical photopolymerization pathway. The following power densities were used (1.2 mW/cm^2, 2.0 mW/cm², 4.0 mW/cm^2, 8.0 mW/cm^2 and 16.0 mW/cm^2). For each power density, t_T was determined in order to perform the near-field experiments at 90% t_T (**Figure S8**). The corresponding threshold time results are 2.4 s, 1.5 s, 0.50 s, 0.23 s and 0.14 s. **Figure 6a** shows TEM images of typical NPs after LSPR polymerization for each power density (see **Figure S9** to **S12** for more TEM images).
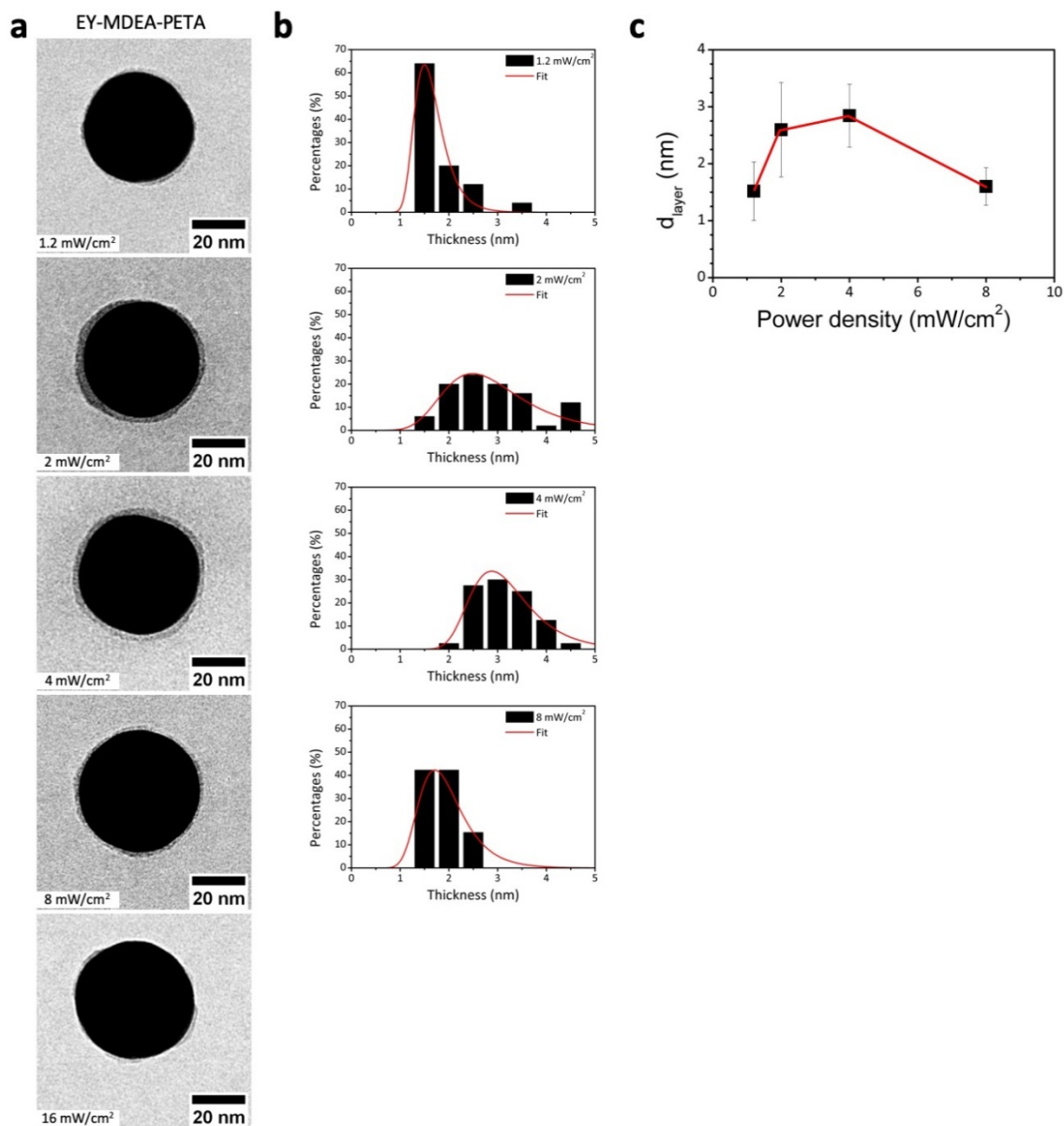
Figure 6: (a) TEM images of 43 nm Au NPs after irradiation with the formulation EY-MDEA-PETA at 1.2 mW/cm², 2.0 mW/cm², 4.0 mW/cm², 8.0 mW/cm² and 16 mW/cm². (b) Histogram of the polymer shell thickness d_{layer} associated with the irradiation conditions used. (c) Evolution of d_{layer} with the power density. The vertical bars represent the standard deviation.

As shown in **Figure 6a**, a layer of polymer surrounding Au NPs is observed after irradiation under each different power conditions except in the case of 16 mW/cm². In addition, we noted a very good uniformi-

ty of the results since at least 90% of the NPs have a homogeneous polymer shell layer. At 16 mW/cm^2, the proportion of NPs with a continuous layer dropped to approximately 20%. For the latter irradiance, the predominant structures observed are irregular polymer nanofragments at the surface of the NPs, as shown in the bottom of **Figure 6a**. This surprisingly shows a less efficient polymerization at high irradiance. For other samples, the thickness distribution and mean thickness (denoted as d_{layer}) were determined and plotted in **Figure 6b** and **6c**, respectively**.** Between 1.2 mW/cm^2 and 4.0 mW/cm^2, d_{layer} increases from 1.5 nm to 2.8 nm. At 8.0 mW/cm^2, this value decreases to 1.5 nm. The efficiency of the polymerization process can be directly correlated to the polymerized thickness. This means that the polymerization efficiency increases first with power, until 4.0 mW/cm^2, and then decreases for higher powers. This behavior is in agreement with a previous study carried out using AFM as a characterization technique.[28] The advantage here is to be able to confirm the results on a wide population of NPs (typically 40 NPs for each irradiation condition). The dependence of the polymerization yield versus incident power reveals two different regimes. At low power density (< 4.0 mW/cm^2), the process is controlled by oxygen quenching. Indeed, to reach the polymerization threshold, the local concentration of radicals must be sufficient to consume the oxygen initially present, which acts as an inhibitor. A low light intensity corresponds to a long irradiation time (the irradiation time is divided by 5 when the power is tuned from 1.2 to 4.0 mW/cm^2), which allows the replenishment of oxygen by diffusion from the formulation. When the light intensity is higher, the reaction time necessary to reach the polymerization threshold decreases, and therefore, the oxygen replenishment is less efficient, resulting in higher polymerization efficiency, as observed here. This phenomenon is also confirmed by the evolution of the threshold dose measured at a macroscopic scale (**Figure S8**).

The decrease in efficiency for the highest powers is less expected although already previously observed.[28] This corresponds to a phenomenon that does not happen at the macroscopic or microscopic scale but only for nanometric scale polymerization resulting from near field excitation conditions. This phenomenon can be explained by the contribution of the diffusion of the dye in the near-field zone to initiate the polymerization reaction with a sufficient probability to obtain a continuous polymer layer at the surface of the NPs.

This is due to the very low number of dye molecules in the near-field volume. Based on the analysis of a large number of particles, this series of experiments confirms this hypothesis and makes it possible to add further support to the photochemical origin of the reactions involved.

We can advance two alternative explanations: one of them is triplet annihilation effects, as we recently reported with another photopolymer system.[75] These effects are observed when locally and temporally, the concentration of triplet states (that are involved in photopolymerization) are in such a concentration that the probability of reaction between 2 triplets becomes important and must be considered. The effect of the interaction between 2 triplets is globally equivalent to a deactivation with respect to the polymerization reaction, hence the notion of annihilation. These effects are obtained under strong light flux. However, in our experimental conditions, this phenomenon does not seem to be preponderant because the light flux remains at a reasonable level and the concentration of dye is limited. A second possibility may be the production of singlet oxygen from triplet oxygen on the surface of metallic nanoparticles under visible light irradiation. Such a phenomenon has been described recently.[76] Triplet oxygen is a powerful oxidant that could degrade the dye in the vicinity of the nanoparticles, which would reduce the efficiency of polymerization under high light flux.

Another way to prove the photochemical origin of the polymerization is to use another photoinitiator system that absorbs at the very same excitation wavelength (532 nm) but follows another mechanism. The EY-MDEA system reacts through a Norrish type II mechanism. We propose here to compare the process with an organo-titanocene, Cp_2TiCl_2 (**Figure 1b**), in the formulation instead of the EY-MDEA system. This photoinitiator can be excited at 532 nm, but its chemical nature and mechanism (Norrish I, e.g. homolytic photolysis of the molecule) are completely different,[77,78] and it is therefore of interest to be compared to the EY-MDEA system.

Since the absorption of Cp_2TiCl_2 is weaker than the absorption of EY at 532 nm (**Figure S13**), the polymerization time is longer than for EY-MDEA formulation for a given power density. As shown in **Figure S14**, at 2.0 mW/cm^2, the value of t_T for a formulation Cp_2TiCl_2-PETA is 56 s (for a concentration in Cp_2TiCl_2: 0.3 wt. %)
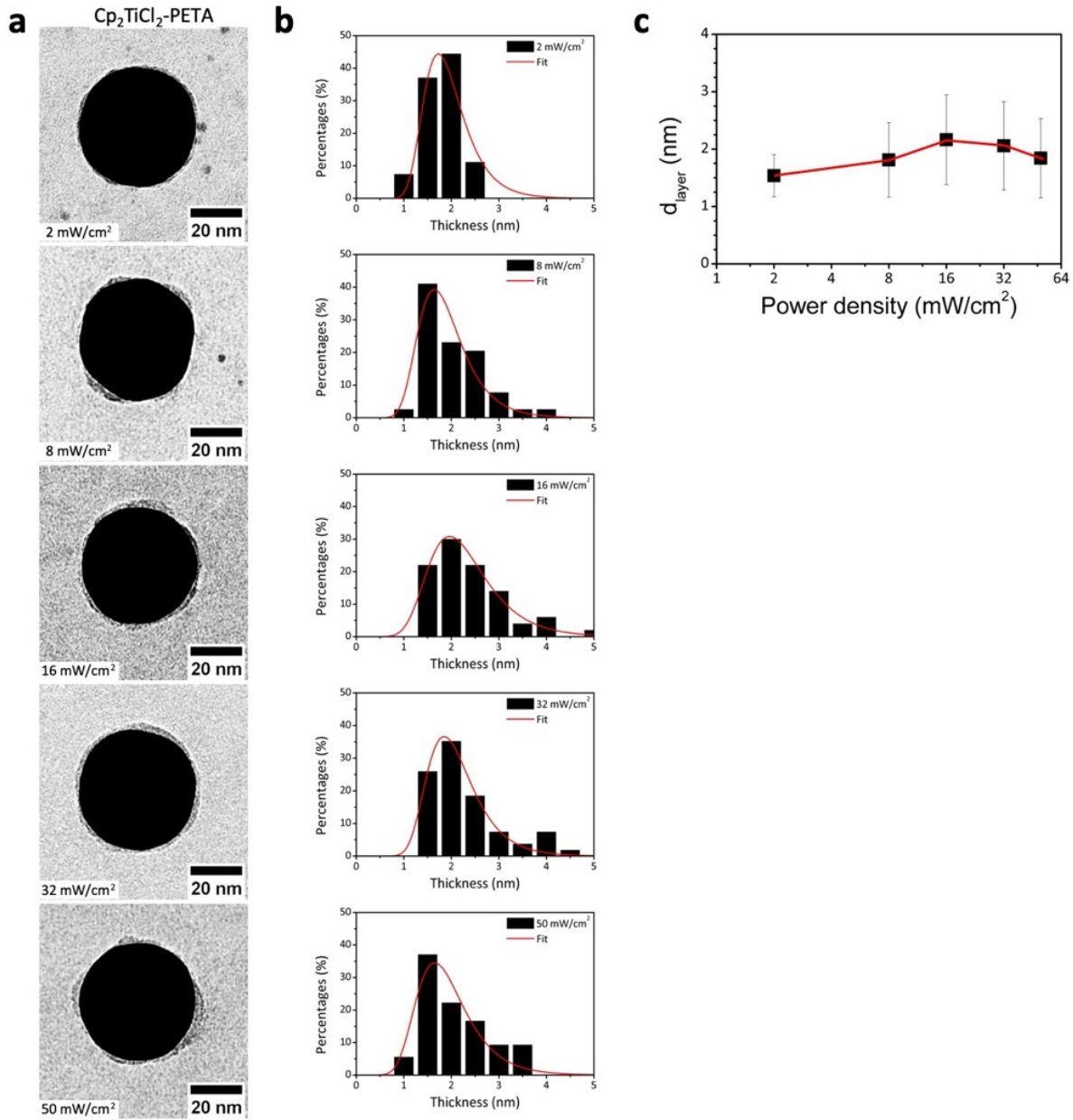
Figure 7: (a) TEM images of 43 nm Au NPs after irradiation with the formulation Cp_2TiCl_2-PETA at 2.0 mW/cm^2, 8.0 mW/cm^2, 16 mW/cm^2, 32 mW/cm^2 and 50 mW/cm^2. (b) Histogram of the polymer shell thickness d_{layer} associated with irradiation conditions used. (c) Evolution of the d_{layer} with the power density. The vertical bars represent the standard deviation.

A Cp_2TiCl_2-PETA formulation was thus used for LSPR polymerization at 2.0 mW/cm^2, 8.0 mW/cm^2, 16 mW/cm^2, 32 mW/cm^2 and 50 mW/cm^2 (90% of t_T for each condition). TEM images of NPs after photopolymerization are shown in **Figure 7a**. A polymer layer can be observed on Au NPs, showing that optical near-field photopolymerization can be triggered with this photoinitiating system. For the Cp_2TiCl_2-PETA system, the values of the d_{layer} were measured from the histograms (**Figure 7b)**, and the evolution of the d_{layer} with the power densities was plotted **(Figure 7c)**. The mean thickness d_{layer} at 2.0 mW/cm^2 is 1.5 nm and increases to 2.2 nm at 32 mW/cm^2. Then, it decreases to 1.9 nm at 50 mW/cm^2. This trend is similar to that observed with the formulation EY-MDEA-PETA and can be explained by the same reasons described above, confirming the photochemical nature of the polymerization.

Finally, as a final formulation composition parameter, the monomer was also changed to evaluate the influence of viscosity on the efficiency of LSPR polymerization. A formulation was prepared by replacing PETA with another trifunctional monomer, TMPTA (**Figure 8a**), which exhibits a viscosity lower than that of PETA (106 cPs vs 800 cPs at 25°C). EY and MDEA were used as photoinitiators, with the same concentrations as for the PETA formulations. The threshold time t_T at 2.0 mW/cm^2 for this formulation was found to be slightly higher than that for PETA (2.6 s), which can be explained by the loss of hydrogen bonding between the monomer and polymer chains. TEM images of Au NPs after a near-field experiment at 90% t_T and at 2.0 mW/cm^2 with the formulation EY-MDEA-TMPTA are shown in **Figure 8b**.
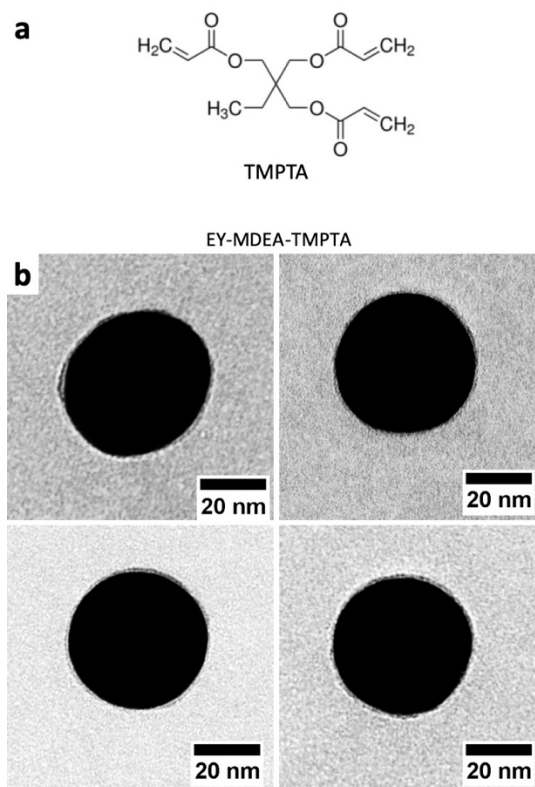
Figure 8: (a) Molecular structure of TMPTA. (b) TEM images of 43 nm Au NPs after irradiation with the formulation EY-MDEA-TMPTA (EY: 0.5 wt %; MDEA: 4 wt %).

As depicted in **Figure 8b**, LSPR polymerization occurs with TMPTA as a monomer. However, the thickness of the polymer shell layer (d_{layer}) is lower when using TMPTA as the monomer formulation. The viscosity can have an impact at different levels of the photopolymerization kinetic pathway, and the overall effect can be either a decrease or an increase in the polymerization efficiency. In the present case, oxygen plays an important role and the low viscosity monomer (TMPTA) favors the diffusion of oxygen. This may thus account for a decrease in the efficiency of the polymerization. In any case, this experiment demonstrates that the process is not limited to one monomer. It can be extended to different acrylate monomers with different physicochemical properties, which is interesting for practical applications.
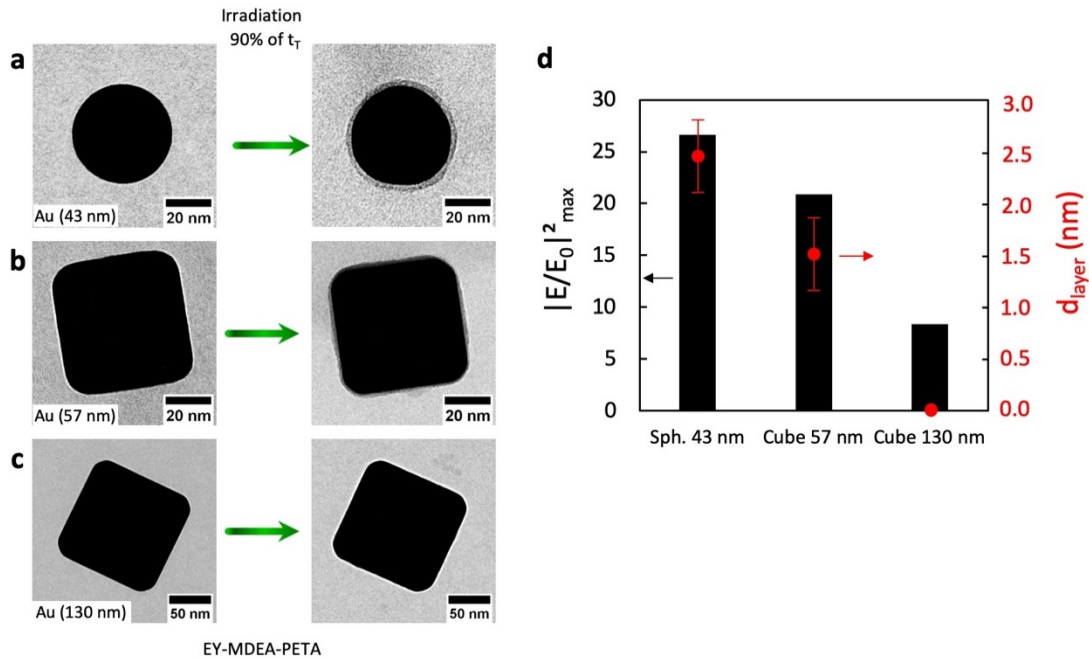
Figure 9: (a) TEM images of 43 nm Au nanospheres before and after irradiation at 90% t_T at 2.0 mW/cm^2. (b) TEM images of 57 nm Au nanocubes before and after irradiation at 90% t_T at 2.0 mW/cm^2. (c) TEM images of 130 nm Au nanocubes before and after irradiation at 90% t_T at 8.0 mW/cm^2. (d) Calculated near-field intensity enhancement ($|E/E_0|^2_{max}$) for the nanoobjects cited above and associated thickness of the induced polymer layer following irradiation (photopolymer: EY-MDEA-PETA).

As a last proof of the photochemical origin of LSPR polymerization, we propose in this last set of experiments to discuss the role of the nanoobject geometry. In particular, photochemical polymerization should be more efficient when the optical near-field intensity enhancement is maximum at the excitation wavelength. The spherical Au NPs used so far were thus compared to Au nanocubes (57 and 130 nm) in photopolymerization experiments. As shown in **Figure 9d**, the optical near-field intensity enhancements $|E/E_0|^2_{max}$ evaluated by BEM simulation at a wavelength of 532 nm are resp. 26.6, 20.9 and 8.9 for 43 nm sphere, 57 nm cubes and 130 nm cubes. The decrease of the intensity enhancements comes from a progressive mismatch between the excitation and plasmon resonance wavelengths of the cubic objects (see Supporting information for details, **Figures S17**, **S18 S19 and S20**). The NPs were used under the same

conditions as the Au nanospheres: after deposition on the TEM grid, irradiation was performed at 90% t_T and at 2.0 mW/cm^2 and 8.0 mW/cm^2 for the 130 nm nanocubes using the reference formulation (EY-MDEA-PETA).

For the 57 nm cubes, the TEM characterization revealed a thin layer of polymer of 1.5 nm (**Figure 9b** and **Figure S15**). The polymer layer was thus significantly thinner than that measured for the 43 nm Au nanospheres (**Figure 3a**). However, the presence of this layer confirmed that the electromagnetic field enhancement at the vicinity of the NP was high enough to locally overpass the polymerization threshold and thus initiate polymerization.

The second cubes tested were 130 nm Au nanocubes (**Figure 9c** and **Figure S16**). Their plasmon resonance was redshifted, corresponding to a weak overlap with the laser irradiation wavelength, which accounts for the weaker field exaltation. Experimental extinction spectra of NPs in solution in water and simulated spectra of the NPs on the Si$_3$N$_4$ substrate, surrounded by the formulation are given in **Figure S20**. The TEM images shown in **Figure 9c** and **Figure S16** show that no polymer around the 130 nm Au nanocubes was formed. A low enhancement factor (< 10) did not allow the start of the polymerization at the nanoscale. The Au surface and photopolymer being exactly the same, it can be concluded that photopolymerization is difficult to observe with low exaltation, though the enhancement factor allows to overpass the polymerization threshold. This result is probably due to the very low volume excited. In such conditions, the limited number of dye molecules and the easy diffusion of inhibitor from the surrounding significantly increase the polymerization threshold at the nanoscale.

However, we thus confirm that the efficiency of the LSRP polymerization is correlated to the optical near-field intensity enhancement, which reinforces the conclusion of a photochemical mechanism driven by the local exaltation of the electromagnetic field in the near field.

Conclusion

A new methodology based on the use of transmission electron microscopy allowed us to study in depth the mechanisms of LSPR polymerization. The chosen irradiation conditions can be qualified as mild (few

mW/cm^2), and the results are studied for a particular physicochemical system (EY-MDEA-PETA) that polymerizes, in the far field, at the wavelength used by following a radical mechanism.

Under such conditions, it is possible, by studying the impact of the main parameters of the system, to prove the photochemical nature of the process and to confirm that the mechanism is therefore linked to the local exaltation of the electromagnetic field, which makes it possible to locally exceed the polymerization threshold. The photochemical nature is also attested by the overlap between the spatial distribution of the field and the distribution of the polymer, as demonstrated by TEM in tomography mode. The possibility of changing the photoinitiator system while maintaining equivalent results is another proof that confirms this mechanism. The power dependence also corresponds to a photochemical process.

A process using hot carriers, particularly through the holes generated on the surface of the particle, might also be possible but is shown to be much less efficient (by a factor of 10) than the photochemical process. It can be observed when the dye is removed from the formulation. A more in-depth study of these phenomena could be envisaged in the future by coupling with studies in time-resolved spectroscopy and by using electron/hole scavengers to promote polymerization phenomena versus electron-hole recombination.

Thermoplasmonic effects, on the other hand, are excluded under our conditions, given the power densities used, the low density of NPs and the temperatures needed to initiate thermal polymerization.

Finally, we highlight that the proposed photopolymer is an excellent probe to study the coupling between metallic nanoobjects and organic molecules at the nanometric scale. By developing this methodology based on TEM, we have at our disposal an excellent tool to study in detail the influence of the chemical, physicochemical and physical parameters involved. In addition to the advances in the understanding of the phenomena involved in the preparation of HNPs, this study allows us to shed light on the coupling mechanisms between metallic nanostructures and organic matter. These results can be applied to other photochemical systems (photoisomerization, photocatalysis, etc.).

Supporting information

We provide in Supporting Information the schematics of the optical setup (S1) and photopoly-merization mechanism (S2), TEM images of reference metal and hybrid nanoparticles prepared with different conditions (S3 to S7, S9 to S12, S15 and S16). Experimental data about the formu-lations are given in S8 and S14 (photopolymerization thresholds) and S13 (UV-vis spectra). BEM simulations and maps of the electric field are given in S17 to S19. Extinction spectra of the nanoparticles used in this study (experimental and BEM simulations) are given in S20.

References

(1)   Anker, J. N.; Hall, W. P.; Lyandres, O.; Shah, N. C.; Zhao, J.; Van Duyne, R. P. Biosensing with Plasmonic Nanosensors. *Nat. Mater.* **2008**, *7* (6), 442–453. https://doi.org/10.1038/nmat2162.

(2)   De, M.; Ghosh, P. S.; Rotello, V. M. Applications of Nanoparticles in Biology. *Adv. Mater.* **2008**, *20* (22), 4225–4241. https://doi.org/10.1002/adma.200703183.

(3)   Arvizo, R. R.; Miranda, O. R.; Thompson, M. A.; Pabelick, C. M.; Bhattacharya, R.; Robertson, J. D.; Rotello, V. M.; Prakash, Y. S.; Mukherjee, P. Effect of Nanoparticle Surface Charge at the Plasma Membrane and Beyond. *Nano Lett.* **2010**, *10* (7), 2543–2548. https://doi.org/10.1021/nl101140t.

(4)   Barchanski, A.; Taylor, U.; Klein, S.; Petersen, S.; Rath, D.; Barcikowski, S. Golden Perspective: Application of Laser-Generated Gold Nanoparticle Conjugates in Reproductive Biology: Gold Nanoparticles in Reproductive Biology. *Reprod. Domest. Anim.* **2011**, *46*, 42–52. https://doi.org/10.1111/j.1439-0531.2011.01844.x.

(5)   Moyano, D. F.; Rotello, V. M. Nano Meets Biology: Structure and Function at the Nanoparticle Interface. *Langmuir* **2011**, *27* (17), 10376–10385. https://doi.org/10.1021/la2004535.

(6)   Komalam, A.; Muraleegharan, L. G.; Subburaj, S.; Suseela, S.; Babu, A.; George, S. Designed Plasmonic Nanocatalysts for the Reduction of Eosin Y: Absorption and Fluorescence Study. *Int. Nano Lett.* **2012**, *2* (1). https://doi.org/10.1186/2228-5326-2-26.

(7)   Sambur, J. B.; Chen, P. Approaches to Single-Nanoparticle Catalysis. *Annu. Rev. Phys. Chem.* **2014**, *65* (1), 395–422. https://doi.org/10.1146/annurev-physchem-040513-103729.

(8)   Deraedt, C.; Astruc, D. "Homeopathic" Palladium Nanoparticle Catalysis of Cross Carbon-Carbon Coupling Reactions. *Acc. Chem. Res.* **2014**, *47* (2), 494–503. https://doi.org/10.1021/ar400168s.

(9)   Kuehn, S.; Hakanson, U.; Rogobete, L.; Sandoghdar, V. On-Command Enhancement of Single Molecule Fluorescence Using a Gold Nanoparticle as an Optical Nano-Antenna. *Phys. Rev. Lett.* **2006**, *97* (1), 017402. https://doi.org/10.1103/PhysRevLett.97.017402.

(10)   Pinchuk, A. O.; Schatz, G. C. Nanoparticle Optical Properties: Far- and near-Field Electrodynamic Coupling in a Chain of Silver Spherical Nanoparticles. *Mater. Sci. Eng. B* **2008**, *149* (3), 251–258. https://doi.org/10.1016/j.mseb.2007.09.078.

(11)   Quinten, M. *Optical Properties of Nanoparticle Systems: Mie and Beyond*; Wiley-VCH Verlag GmbH & Co. KGaA: Weinheim, Germany, 2011. https://doi.org/10.1002/9783527633135.

(12)   *Near-Field Optics and Surface Plasmon Polaritons*; Kawata, S., Ed.; Topics in Applied Physics; Springer Berlin Heidelberg: Berlin, Heidelberg, 2001; Vol. 81. https://doi.org/10.1007/3-540-44552-8.

(13)   Fu, Q.; Sun, W. Mie Theory for Light Scattering by a Spherical Particle in an Absorbing Medium. *Appl. Opt.* **2001**, *40* (9), 1354. https://doi.org/10.1364/AO.40.001354.

(14)   Webb, J. A.; Bardhan, R. Emerging Advances in Nanomedicine with Engineered Gold Nanostructures. *Nanoscale* **2014**, *6* (5), 2502. https://doi.org/10.1039/c3nr05112a.

(15)   Scaiano, J. C.; Stamplecoskie, K. Can Surface Plasmon Fields Provide a New Way to Photosensitize Organic Photoreactions? From Designer Nanoparticles to Custom Applications. *J. Phys. Chem. Lett.* **2013**, *4* (7), 1177–1187. https://doi.org/10.1021/jz400002a.

(16) Bagheri, A.; Arandiyan, H.; Adnan, N. N. M.; Boyer, C.; Lim, M. Controlled Direct Growth of Polymer Shell on Upconversion Nanoparticle Surface via Visible Light Regulated Polymerization. *Macromolecules* **2017**, *50* (18), 7137–7147. https://doi.org/10.1021/acs.macromol.7b01405.

(17) del Pino, P.; Yang, F.; Pelaz, B.; Zhang, Q.; Kantner, K.; Hartmann, R.; Martinez de Baroja, N.; Gallego, M.; Möller, M.; Manshian, B. B.; Soenen, S. J.; Riedel, R.; Hampp, N.; Parak, W. J. Basic Physicochemical Properties of Polyethylene Glycol Coated Gold Nanoparticles That Determine Their Interaction with Cells. *Angew. Chem. Int. Ed.* **2016**, *55* (18), 5483–5487. https://doi.org/10.1002/anie.201511733.

(18) Abadeer, N. S.; Brennan, M. R.; Wilson, W. L.; Murphy, C. J. Distance and Plasmon Wavelength Dependent Fluorescence of Molecules Bound to Silica-Coated Gold Nanorods. *ACS Nano* **2014**, *8* (8), 8392–8406. https://doi.org/10.1021/nn502887j.

(19) Bai, M.; Huang, S.; Xu, S.; Hu, G.; Wang, L. Fluorescent Nanosensors via Photoinduced Polymerization of Hydrophobic Inorganic Quantum Dots for the Sensitive and Selective Detection of Nitroaromatics. *Anal. Chem.* **2015**, *87* (4), 2383–2388. https://doi.org/10.1021/ac504322s.

(20) Sih, B. C.; Wolf, M. O. Metal Nanoparticle-Conjugated Polymer Nanocomposites. *Chem. Commun.* **2005**, No. 27, 3375. https://doi.org/10.1039/b501448d.

(21) Anyaogu, K. C.; Cai, X.; Neckers, D. C. Gold Nanoparticle Photopolymerization of Acrylates. *Macromolecules* **2008**, *41* (23), 9000–9003. https://doi.org/10.1021/ma801391p.

(22) Balan, L.; Malval, J.-P.; Schneider, R.; Le Nouen, D.; Lougnot, D.-J. In-Situ Fabrication of Polyacrylate–Silver Nanocomposite through Photoinduced Tandem Reactions Involving Eosin Dye. *Polymer* **2010**, *51* (6), 1363–1369. https://doi.org/10.1016/j.polymer.2009.05.003.

(23) Ehlert, S.; Taheri, S. M.; Pirner, D.; Drechsler, M.; Schmidt, H.-W.; Förster, S. Polymer Ligand Exchange to Control Stabilization and Compatibilization of Nanocrystals. *ACS Nano* **2014**, *8* (6), 6114–6122. https://doi.org/10.1021/nn5014512.

(24) Choueiri, R. M.; Galati, E.; Thérien-Aubin, H.; Klinkova, A.; Larin, E. M.; Querejeta-Fernández, A.; Han, L.; Xin, H. L.; Gang, O.; Zhulina, E. B.; Rubinstein, M.; Kumacheva, E. Surface Patterning of Nanoparticles with Polymer Patches. *Nature* **2016**, *538* (7623), 79–83. https://doi.org/10.1038/nature19089.

(25) Kherbouche, I.; Luo, Y.; Félidj, N.; Mangeney, C. Plasmon-Mediated Surface Functionalization: New Horizons for the Control of Surface Chemistry on the Nanoscale. *Chem. Mater.* **2020**, *32* (13), 5442–5454. https://doi.org/10.1021/acs.chemmater.0c00921.

(26) Ueno, K.; Juodkazis, S.; Shibuya, T.; Yokota, Y.; Mizeikis, V.; Sasaki, K.; Misawa, H. Nanoparticle Plasmon-Assisted Two-Photon Polymerization Induced by Incoherent Excitation Source. *J. Am. Chem. Soc.* **2008**, *130* (22), 6928–6929. https://doi.org/10.1021/ja801262r.

(27) Deeb, C.; Bachelot, R.; Plain, J.; Baudrion, A.-L.; Jradi, S.; Bouhelier, A.; Soppera, O.; Jain, P. K.; Huang, L.; Ecoffet, C.; Balan, L.; Royer, P. Quantitative Analysis of Localized Surface Plasmons Based on Molecular Probing. *ACS Nano* **2010**, *4* (8), 4579–4586. https://doi.org/10.1021/nn101017b.

(28) Deeb, C.; Ecoffet, C.; Bachelot, R.; Plain, J.; Bouhelier, A.; Soppera, O. Plasmon-Based Free-Radical Photopolymerization: Effect of Diffusion on Nanolithography Processes. *J. Am. Chem. Soc.* **2011**, *133* (27), 10535–10542. https://doi.org/10.1021/ja201636y.

(29) Walker, J. M.; Gou, L.; Bhattacharyya, S.; Lindahl, S. E.; Zaleski, J. M. Photothermal Plasmonic Triggering of Au Nanoparticle Surface Radical Polymerization. *Chem. Mater.* **2011**, *23* (23), 5275–5281. https://doi.org/10.1021/cm202741p.

(30) Kameche, F.; Heni, W.; Telitel, S.; Ge, D.; Vidal, L.; Dumur, F.; Gigmes, D.; Lalevée, J.; Marguet, S.; Douillard, L.; Fiorini-Debuisschert, C.; Bachelot, R.; Soppera, O. Plasmon-Triggered Living Photopolymerization for Elaboration of Hybrid Polymer/Metal Nanoparticles. *Mater. Today* **2020**. https://doi.org/10.1016/j.mattod.2020.03.023.

(31) Guselnikova, O.; Marque, S. R. A.; Tretyakov, E. V.; Mares, D.; Jerabek, V.; Audran, G.; Joly, J.-P.; Trusova, M.; Svorcik, V.; Lyutakov, O.; Postnikov, P. Unprecedented Plasmon-Induced Nitroxide-Mediated Polymerization (PI-NMP): A Method for Preparation of Functional Surfaces. *J. Mater. Chem. A* **2019**, *7* (20), 12414–12419. https://doi.org/10.1039/C9TA01630A.

(32) Erzina, M.; Guselnikova, O.; Postnikov, P.; Elashnikov, R.; Kolska, Z.; Miliutina, E.; Švorčík, V.; Lyutakov, O. Plasmon-Polariton Induced, "from Surface" RAFT Polymerization, as a Way toward Creation of Grafted Polymer Films with Thickness Precisely Controlled by Self-Limiting Mechanism. *Adv. Mater. Interfaces* **2018**, *5* (22), 1801042. https://doi.org/10.1002/admi.201801042.

(33) Wang, Y.; Wang, S.; Zhang, S.; Scherman, O. A.; Baumberg, J. J.; Ding, T.; Xu, H. Plasmon-Directed Polymerization: Regulating Polymer Growth with Light. *Nano Res.* **2018**, *11* (12), 6384–6390. https://doi.org/10.1007/s12274-018-2163-0.

(34) Ding, T.; Mertens, J.; Lombardi, A.; Scherman, O. A.; Baumberg, J. J. Light-Directed Tuning of Plasmon Resonances via Plasmon-Induced Polymerization Using Hot Electrons. *ACS Photonics* **2017**, *4* (6), 1453–1458. https://doi.org/10.1021/acsphotonics.7b00206.

(35) Kim, M.; Lin, M.; Son, J.; Xu, H.; Nam, J.-M. Hot-Electron-Mediated Photochemical Reactions: Principles, Recent Advances, and Challenges. *Adv. Opt. Mater.* **2017**, *5* (15), 1700004. https://doi.org/10.1002/adom.201700004.

(36) Gellé, A.; Jin, T.; de la Garza, L.; Price, G. D.; Besteiro, L. V.; Moores, A. Applications of Plasmon-Enhanced Nanocatalysis to Organic Transformations. *Chem. Rev.* **2020**, *120* (2), 986–1041. https://doi.org/10.1021/acs.chemrev.9b00187.

(37) Nguyen, V.-Q.; Ai, Y.; Martin, P.; Lacroix, J.-C. Plasmon-Induced Nanolocalized Reduction of Diazonium Salts. *ACS Omega* **2017**, *2* (5), 1947–1955. https://doi.org/10.1021/acsomega.7b00394.

(38) Nguyen, M.; Lamouri, A.; Salameh, C.; Lévi, G.; Grand, J.; Boubekeur-Lecaque, L.; Mangeney, C.; Félidj, N. Plasmon-Mediated Chemical Surface Functionalization at the Nanoscale. *Nanoscale* **2016**, *8* (16), 8633–8640. https://doi.org/10.1039/C6NR00744A.

(39) Kowalska, E.; Abe, R.; Ohtani, B. Visible Light-Induced Photocatalytic Reaction of Gold-Modified Titanium(IV) Oxide Particles: Action Spectrum Analysis. *Chem Commun* **2009**, No. 2, 241–243. https://doi.org/10.1039/B815679D.

(40) Kowalska, E.; Mahaney, O. O. P.; Abe, R.; Ohtani, B. Visible-Light-Induced Photocatalysis through Surface Plasmon Excitation of Gold on Titania Surfaces. *Phys. Chem. Chem. Phys.* **2010**, *12* (10), 2344. https://doi.org/10.1039/b917399d.

(41) Lee, S. W.; Hong, J. W.; Lee, H.; Wi, D. H.; Kim, S. M.; Han, S. W.; Park, J. Y. The Surface Plasmon-Induced Hot Carrier Effect on the Catalytic Activity of CO Oxidation on a Cu_2O/Hexoctahedral Au Inverse Catalyst. *Nanoscale* **2018**, *10* (23), 10835–10843. https://doi.org/10.1039/C8NR00555A.

(42) Pensa, E.; Gargiulo, J.; Lauri, A.; Schlücker, S.; Cortés, E.; Maier, S. A. Spectral Screening of the Energy of Hot Holes over a Particle Plasmon Resonance. *Nano Lett.* **2019**, *19* (3), 1867–1874. https://doi.org/10.1021/acs.nanolett.8b04950.

(43) Minamimoto, H.; Toda, T.; Futashima, R.; Li, X.; Suzuki, K.; Yasuda, S.; Murakoshi, K. Visualization of Active Sites for Plasmon-Induced Electron Transfer Reactions Using Photoelectrochemical Polymerization of Pyrrole. *J. Phys. Chem. C* **2016**, *120* (29), 16051–16058. https://doi.org/10.1021/acs.jpcc.5b12727.

(44) Baffou, G.; Rigneault, H. Femtosecond-Pulsed Optical Heating of Gold Nanoparticles. *Phys. Rev. B* **2011**, *84* (3). https://doi.org/10.1103/PhysRevB.84.035415.

(45) Hodak, J. H.; Martini, I.; Hartland, G. V. Spectroscopy and Dynamics of Nanometer-Sized Noble Metal Particles. *J. Phys. Chem. B* **1998**, *102* (36), 6958–6967. https://doi.org/10.1021/jp9809787.

(46) Link, S.; Burda, C.; Mohamed, M. B.; Nikoobakht, B.; El-Sayed, M. A. Laser Photothermal Melting and Fragmentation of Gold Nanorods: Energy and Laser Pulse-Width Dependence. *J. Phys. Chem. A* **1999**, *103* (9), 1165–1170. https://doi.org/10.1021/jp983141k.

(47) Link, S.; El-Sayed, M. A. Shape and Size Dependence of Radiative, Non-Radiative and Photothermal Properties of Gold Nanocrystals. *Int. Rev. Phys. Chem.* **2000**, *19* (3), 409–453. https://doi.org/10.1080/01442350050034180.

(48) Hirsch, L. R.; Stafford, R. J.; Bankson, J. A.; Sershen, S. R.; Rivera, B.; Price, R. E.; Hazle, J. D.; Halas, N. J.; West, J. L. Nanoshell-Mediated near-Infrared Thermal Therapy of Tumors under Magnetic Resonance Guidance. *Proc. Natl. Acad. Sci.* **2003**, *100* (23), 13549–13554. https://doi.org/10.1073/pnas.2232479100.

(49) Govorov, A. O.; Richardson, H. H. Generating Heat with Metal Nanoparticles. *Nano Today* **2007**, *2* (1), 30–38. https://doi.org/10.1016/S1748-0132(07)70017-8.

(50) Fedoruk, M.; Meixner, M.; Carretero-Palacios, S.; Lohmüller, T.; Feldmann, J. Nanolithography by Plasmonic Heating and Optical Manipulation of Gold Nanoparticles. *ACS Nano* **2013**, *7* (9), 7648–7653. https://doi.org/10.1021/nn402124p.

(51) Stamplecoskie, K. G.; Fasciani, C.; Scaiano, J. C. Dual-Stage Lithography from a Light-Driven, Plasmon-Assisted Process: A Hierarchical Approach to Subwavelength Features. *Langmuir* **2012**, *28* (30), 10957–10961. https://doi.org/10.1021/la301728r.

(52) Rodríguez-Fernández, J.; Pérez-Juste, J.; Mulvaney, P.; Liz-Marzán, L. M. Spatially-Directed Oxidation of Gold Nanoparticles by Au(III)–CTAB Complexes. *J. Phys. Chem. B* **2005**, *109* (30), 14257–14261. https://doi.org/10.1021/jp052516g.

(53) Deeb, C.; Zhou, X.; Miller, R.; Gray, S. K.; Marguet, S.; Plain, J.; Wiederrecht, G. P.; Bachelot, R. Mapping the Electromagnetic Near-Field Enhancements of Gold Nanocubes. *J. Phys. Chem. C* **2012**, *116* (46), 24734–24740. https://doi.org/10.1021/jp304647e.

(54) Haggui, M.; Dridi, M.; Plain, J.; Marguet, S.; Perez, H.; Schatz, G. C.; Wiederrecht, G. P.; Gray, S. K.; Bachelot, R. Spatial Confinement of Electromagnetic Hot and Cold Spots in Gold Nanocubes. *ACS Nano* **2012**, *6* (2), 1299–1307. https://doi.org/10.1021/nn2040389.

(55) Ruan, Q.; Shao, L.; Shu, Y.; Wang, J.; Wu, H. Growth of Monodisperse Gold Nanospheres with Diameters from 20 Nm to 220 Nm and Their Core/Satellite Nanostructures. *Adv. Opt. Mater.* **2014**, *2* (1), 65–73. https://doi.org/10.1002/adom.201300359.

(56) Ibn El Ahrach, H.; Bachelot, R.; Vial, A.; Lérondel, G.; Plain, J.; Royer, P.; Soppera, O. Spectral Degeneracy Breaking of the Plasmon Resonance of Single Metal Nanoparticles by Nanoscale Near-Field Photopolymerization. *Phys. Rev. Lett.* **2007**, *98* (10). https://doi.org/10.1103/PhysRevLett.98.107402.

(57) Zhou, X.; Soppera, O.; Plain, J.; Jradi, S.; Wei Sun, X.; Volkan Demir, H.; Yang, X.; Deeb, C.; Gray, S. K.; Wiederrecht, G. P.; Bachelot, R. Plasmon-Based Photopolymerization: Near-Field Probing, Advanced Photonic Nanostructures and Nanophotochemistry. *J. Opt.* **2014**, *16* (11), 114002. https://doi.org/10.1088/2040-8978/16/11/114002.

(58) Soppera, O.; Jradi, S.; Lougnot, D. J. Photopolymerization with Microscale Resolution: Influence of the Physico-Chemical and Photonic Parameters. *J. Polym. Sci. Part Polym. Chem.* **2008**, *46* (11), 3783–3794. https://doi.org/10.1002/pola.22727.

(59) Jradi, S.; Soppera, O.; Lougnot, D. J. Fabrication of Polymer Waveguides between Two Optical Fibers Using Spatially Controlled Light-Induced Polymerization. *Appl. Opt.* **2008**, *47* (22), 3987. https://doi.org/10.1364/AO.47.003987.

(60) Croutxé-Barghorn, C.; Soppera, O.; Simonin, L.; Lougnot, D. J. On the Unexpected Role of Oxygen in the Generation of Microlens Arrays with Self-Developing Photopolymers. *Adv. Mater. Opt. Electron.* **2000**, *10* (1), 25–38. https://doi.org/10.1002/1099-0712(200001/02)10:1<25::AID-AMO395>3.0.CO;2-I.

(61) Jradi, S.; Soppera, O.; Lougnot, D. J. Analysis of Photopolymerized Acrylic Films by AFM in Pulsed Force Mode. *J. Microsc.* **2008**, *229* (1), 151–161. https://doi.org/10.1111/j.1365-2818.2007.01878.x.

(62) Sundararaman, R.; Narang, P.; Jermyn, A. S.; Goddard III, W. A.; Atwater, H. A. Theoretical Predictions for Hot-Carrier Generation from Surface Plasmon Decay. *Nat. Commun.* **2014**, *5* (1). https://doi.org/10.1038/ncomms6788.

(63) Govorov, A. O.; Zhang, W.; Skeini, T.; Richardson, H.; Lee, J.; Kotov, N. A. Gold Nanoparticle Ensembles as Heaters and Actuators: Melting and Collective Plasmon Resonances. *Nanoscale Res. Lett.* **2006**, *1* (1), 84–90. https://doi.org/10.1007/s11671-006-9015-7.

(64) Baffou, G.; Quidant, R.; Girard, C. Heat Generation in Plasmonic Nanostructures: Influence of Morphology. *Appl. Phys. Lett.* **2009**, *94* (15), 153109. https://doi.org/10.1063/1.3116645.

(65) Baffou, G.; Quidant, R.; García de Abajo, F. J. Nanoscale Control of Optical Heating in Complex Plasmonic Systems. *ACS Nano* **2010**, *4* (2), 709–716. https://doi.org/10.1021/nn901144d.

(66) Baffou, G.; Quidant, R.; Girard, C. Thermoplasmonics Modeling: A Green's Function Approach. *Phys. Rev. B* **2010**, *82* (16). https://doi.org/10.1103/PhysRevB.82.165424.

(67) Honda, M.; Saito, Y.; Smith, N. I.; Fujita, K.; Kawata, S. Nanoscale Heating of Laser Irradiated Single Gold Nanoparticles in Liquid. *Opt. Express* **2011**, *19* (13), 12375. https://doi.org/10.1364/OE.19.012375.

(68) Sanchot, A.; Baffou, G.; Marty, R.; Arbouet, A.; Quidant, R.; Girard, C.; Dujardin, E. Plasmonic Nanoparticle Networks for Light and Heat Concentration. *ACS Nano* **2012**, 6 (4), 3434–3440. https://doi.org/10.1021/nn300470j

(69) Baffou, G.; Quidant, R. Thermo-Plasmonics: Using Metallic Nanostructures as Nano-Sources of Heat: Thermoplasmonics. *Laser Photonics Rev.* **2013**, *7* (2), 171–187. https://doi.org/10.1002/lpor.201200003.

(70) Baffou, G.; Bordacchini, I.; Baldi, A.; Quidant, R. Simple Experimental Procedures to Distinguish Photothermal from Hot-Carrier Processes in Plasmonics. *Light Sci. Appl.* **2020**, *9* (1). https://doi.org/10.1038/s41377-020-00345-0.

(71) Baffou, G.; Berto, P.; Bermúdez Ureña, E.; Quidant, R.; Monneret, S.; Polleux, J.; Rigneault, H. Photoinduced Heating of Nanoparticle Arrays. *ACS Nano* **2013**, *7* (8), 6478–6488. https://doi.org/10.1021/nn401924n.

(72) Kader, M. A.; Bhowmick, A. K. Thermal Ageing, Degradation and Swelling of Acrylate Rubber, Fluororubber and Their Blends Containing Polyfunctional Acrylates. *Polym. Degrad. Stab.* **2003**, *79* (2), 283–295. https://doi.org/10.1016/S0141-3910(02)00292-6.

(73) Muhammad, A.; Mutalib, M. I. A.; Wilfred, C. D.; Murugesan, T.; Shafeeq, A. Viscosity, Refractive Index, Surface Tension, and Thermal Decomposition of Aqueous *N*-Methyldiethanolamine Solutions from (298.15 to 338.15) K. *J. Chem. Eng. Data* **2008**, *53* (9), 2226–2229. https://doi.org/10.1021/je800282a.

(74) de Ávila, S. G.; Logli, M. A.; Matos, J. R. Kinetic Study of the Thermal Decomposition of Monoethanolamine (MEA), Diethanolamine (DEA), Triethanolamine (TEA) and Methyl-diethanolamine (MDEA). *Int. J. Greenh. Gas Control* **2015**, *42*, 666–671. https://doi.org/10.1016/j.ijggc.2015.10.001.

(75) Dika, I.; Diot, F; Bardinal, V; Malval, J.-P.; Ecoffet, C.; Bruyant, A.; Barat, D.; Reig B.; Doucet, J.-B.; Camps, T.; Soppera, O. Near infrared photopolymer for micro-optics applications. *J Polym Sci*. **2020**; 58: 1796-1809. https://doi.org/10.1002/pol.20200106

(76) Huang, Y.-F.; Zhang, M.; Zhao, L.-B.; Feng, J.-M.; Wu, D.-Y.; Ren, B.; Tian, Z.-Q. Activation of Oxygen on Gold and Silver Nanoparticles Assisted by Surface Plasmon Resonances. *Angew. Chem. Int. Ed.* 2014, 53, 2353-2357. https://doi.org/10.1002/anie.201310097

(77) Kopietz, M.; Lechner, M. D.; Steinmeier, D. G.; Marotz, J.; Franke, H.; Krätzig, E. Light-Induced Refractive Index Changes in Polymethylmethacrylate (PMMA) Blocks. *Polym. Photochem.* **1984**, *5* (1–6), 109–119. https://doi.org/10.1016/0144-2880(84)90025-3.

(78) Lückemeyer, T.; Franke, H. Profiles in Volume Phase Holograms in Cp2TiCl2:PMMA. *Appl. Phys. B Photophysics Laser Chem.* **1988**, *46* (2), 157–164. https://doi.org/10.1007/BF00686470.

TOC image